Dalton Transactions

ROYAL SOCIETY OF CHEMISTRY

PAPER

View Article Online
View Journal | View Issue

Cite this: *Dalton Trans.*, 2023, **52**, 16525

Compositionally engineered Cd–Mo–Se alloyed QDs toward photocatalytic H_2O_2 production and Cr(VI) reduction with a detailed mechanism and influencing parameters†

Jyotirmayee Sahu, Sriram Mansingh, Bhagyashree Priyadarshini Mishra, Deeptimayee Prusty and Kulamani Parida *

With the exceptional advantages of safety, greenness, and low cost, photocatalytic H_2O_2 generation has kindled a wonderful spark, although being severely hampered by the terrible photoinduced exciton recombination, migration, and surface decomposition. Here, employing reflux method, the Cd–Mo–Se quantum dots of varying molar ratios of Cd and Mo were synthesized using thioglycolic acid as the capping ligand to regulate their growth. This type of metal alloying promotes rapid charge migration, improves light harvesting, and reduces the rate of charge recombination. The improved optoelectronic properties and boosted activity of Cd-rich ternary CMSe-1 QDs led to the observed exceptional photocatalytic H_2O_2 yield of 1403.5 μmol g^{-1} h^{-1} (solar to chemical conversion efficiency, 0.27%) under visible light, outperforming the other ternary and Se-based QD photocatalysts. Additionally, CMSe-1 shows 93.6% (2 h) hazardous Cr(VI) photoreduction. The enhanced catalytic performance of CMSe-1 corresponds to effective charge carrier separation and transfer efficiency, well supported by PL, TRPL, and electrochemical measurements. Photocatalytic H_2O_2 production was also studied under varying experimental conditions and the scavenger test suggests a superoxide radical intermediate 2-step single electron reduction pathway. The catalyst-assisted Cr(VI) reduction is substantiated by the zero-order kinetics as well as the determination of the pH_{PZC} value. The catalyst can be employed for a maximum of four times while retaining its activity, according to the photostability and reusability test outcomes. This research presents interesting approaches for producing ternary QDs and modified systems for efficient photocatalytic H_2O_2 production and Cr(VI) reduction.

Received 7th August 2023,
Accepted 9th October 2023

DOI: 10.1039/d3dt02555a

rsc.li/dalton

Introduction

H_2O_2 has gained considerable attention for its use as a safe and green oxidant in chemical synthesis, papermaking, disinfection, and wastewater treatment.[1,2] These days, H_2O_2 is also utilized as a fuel in cutting-edge one-compartment fuel cells, having output potentials on par with those of traditional hydrogen fuel cells.[3] At present, anthraquinone oxidation (AQ) is the conventional technique for the commercial synthesis of H_2O_2; however, this approach leads to substantial noxious by-products, toxic solvent use, and extensive energy consumption.[4,5] Additionally, the direct catalytic combination of H_2 and O_2 (such as Pd or Au/Pd) has explosion hazards, whereas the electrochemical method has selectivity issues and hence has not yet been used in industrial production.[6] Considerable effort has been put into investigating the most efficient and environmentally viable technique to substitute the AQ method and meet the diversified demand.[7,8] Photocatalytic H_2O_2 generation is currently viewed as a revolutionary option as far as the environment and sustainability are concerned.[9] However, H_2O_2 is thermodynamically unstable and tends to dismutate backward into H_2O and O_2 which reduces the overall yield which is another challenge. Photocatalytic generation of H_2O_2 is frequently observed when oxygen is permitted to engage with the photocatalyst in the presence of hole-quenching elements (*e.g.*, oxalic acids, alcohols, *etc.*). Typically, the holes (h^+) in the valence band (VB) oxidize H_2O/sacrificial agents to H^+ and O_2/oxidized product, while the electrons (e^-) in the conduction band (CB) with the

Centre for Nanoscience and Nanotechnology, Siksha 'O' Anusandhan (Deemed to be University), Bhubaneswar-751030, Odisha, India.
E-mail: paridakulamani@yahoo.com, kulamaniparida@soa.ac.in, jsahu962016@gmail.com, smansingh908@gmail.com, bhagyashree94dkl@gmail.com, deeptimayee.prusty003@gmail.com; Tel: +91-9776645909

† Electronic supplementary information (ESI) available. See DOI: https://doi.org/10.1039/d3dt02555a

required potential take part in the O_2 reduction reaction (ORR). The O_2 reduction reaction proceeds *via* a single-step two-electron ($O_2 + 2H^+ + 2e^- \rightarrow H_2O_2$, 0.68 V *vs.* NHE) or stepwise single-electron ($O_2 + e^- \rightarrow {}^{\bullet}O_2^-$, −0.33 V *vs.* NHE and ${}^{\bullet}O_2^- + e^- + 2H^+ \rightarrow H_2O_2$, 1.44 V *vs.* NHE) pathway, producing H_2O_2. Hence, it is crucial to pick a photocatalyst with the right band edge potentials, along with improved carrier separation and transfer efficiency to achieve an enhanced activity.[10,11] In this regard, a wide range of photocatalysts including TiO_2, g-C_3N_4, QDs, RGO-based systems, and metal–organic frameworks (MOFs) have been investigated but to touch the target value for the large-scale industrial production of H_2O_2 remains challenging.[12–21]

In addition to this, the release of toxic heavy metal ions, specifically Cr(VI), from industrial wastewater into surface water and groundwater presents a significant risk to both human health and aquatic ecosystem equilibrium.[22] This is primarily due to the considerable solubility of Cr(VI) in water, as well as its substantial carcinogenic and acute toxic properties.[23] However, Cr(III) has been proven to be less hazardous as compared to Cr(VI) due to its limited oxidation characteristics and bioavailability.[24] Significant research interest has been directed towards the development of highly efficient photocatalysts for the reduction of Cr(VI) due to the eco-friendly, renewable, and sustainable nature of the photocatalytic process.[25–28] Out of the many recently reported materials, QD-based photocatalytic systems are promising candidates. They show the maximum absorption range in the visible region because of their multiple electron production with a single photon and band gap tunability concerning particle size.[29–31]

Quantum dots (QDs) are a kind of zero-dimensional photocatalyst with a quantum confinement effect, a greater surface binding potential, tunable optoelectronic properties, and chemical stability that have been extensively explored over the past few years for various photocatalytic applications.[32–35] In this context, the author group has made tremendous advancements and developed potent QDs toward water splitting, N_2 fixation, and environmental pollutant remediation-related applications.[36–39] According to several studies, visible light activates QDs in an aerobic environment and releases superoxide radicals (${}^{\bullet}O_2^-$), which are regarded as one of the crucial intermediates for the production of H_2O_2. Therefore, photocatalytic generation of H_2O_2 employing QDs as a photocatalyst under visible light conditions may be feasible.[40] Moreover, the formation of superoxide radicals by QDs has been reported to give them exceptional selectivity for H_2O_2. However, the efficiency is still below the benchmark for standard applications. As a result, a variety of modification techniques, including doping, heterojunction formation, and defect engineering are frequently followed to increase the activity of photocatalytic H_2O_2 generation on QDs.[41–43] As seminal studies, Xu *et al.* investigated the H_2O_2 production capacity of CdSe QDs that goes *via* the two-electron and one-electron molecular oxygen reduction process. The group then prepared K, P, N, co-doped hollow carbon polyhedron (KPN-HCP) modified CdSe QDs and reported a four-fold increase in H_2O_2 generation due to improved O_2/H_2O surface adsorption, effective electron–hole separation and proton release.[44] In a recent study, Ji *et al.* investigated H_2O_2 production over CdSe-based core/shell QDs and improved their activity (126 mmol L^{-1}/2 h) *via* wavefunction engineering, tunable band alignment, and surface–shell structure design.[17] Alloyed QDs can be synthesized by making composites between binary QDs and other semiconducting materials. By choosing the appropriate alloy composition, the band gap alignment of alloyed QDs can be widely tuned and optimized, which is attributed to the optical bowing effect and their absorption can be extended into the visible region.[45] Alloying Cd and Mo to form ternary Cd–Mo–Se QDs is an efficient way to enhance the photocatalytic efficiency as compared to binary CdSe and $MoSe_2$ QDs by suppressing the exciton recombination rate. The band structure of $Cd_xMo_{1-x}Se$ QDs can be tuned according to the composition of Cd and Mo, which exhibits better performance in photocatalytic H_2O_2 production than CdSe.

In this study, alloyed $Cd_xMo_{1-x}Se$ (CMSe) QDs with a varying content of Cd and Mo along with binary CdSe and $MoSe_2$ QDs were fabricated by the one-step reflux method using an appropriate amount of thioglycolic acid to prevent agglomeration of small sized QDs. The Cd-rich alloyed QDs (CMSe-1, where $x = 0.7$) show superior performance to the Mo-rich alloyed QDs (CMSe-2, where $x = 0.3$) with excellent reusability. The higher the Cd proportion, the wider the band gap in the alloyed QDs, which leads to a lower charge recombination rate and higher band potential, which is in good accordance with the data of PL, M–S plot, and EIS measurements. The prepared QDs were examined towards photocatalytic H_2O_2 production under different reaction conditions and it was found that the activity of CMSe-1 alloyed QDs (1403.5 μmol g^{-1} h^{-1}) outperforms both the binary QDs. Furthermore, CMSe-1 QDs show noticeable efficiency (93.6% in 2 h) in photocatalytic Cr(VI) reduction at low pH. The mechanisms of both H_2O_2 production and Cr(VI) reduction have been studied in detail along with the involvement of active species, which is supported by scavenger tests. The presence of defects plays an important role in increased peroxide formation and Cr(VI) reduction. This investigation paves a new avenue in designing compositionally engineered alloyed QDs for achieving improved catalytic efficiency for various photocatalytic energy and environmental-related applications.

Experimental section

Materials

$Cd(NO_3)_2{\cdot}4H_2O$, $Na_2MoO_4{\cdot}2H_2O$, thioglycolic acid (TGA), $NaBH_4$, KI, and ammonium molybdate were purchased from Merck, India. Selenium powder was purchased from Himedia. All chemicals were of analytical reagent grade, so used as such without any further purification. Throughout the reaction, distilled water was used as a solvent.

Synthesis of Cd–Mo–Se QDs

Binary and alloyed QDs were fabricated by a one pot method by following previously reported literature with slight modification.[46] Briefly, NaHSe solutions as Se precursor were synthesized by dissolving Se powder with $NaBH_4$ in chilled water. 159 mg (4 mmol) of $NaBH_4$ was dissolved in 2 mL of chilled distilled water in a flask, followed by the addition of 158 mg (2 mmol) of Se powder. Immediately the flask was placed into an ice bath and H_2 gas was bubbled for approximately 60 to 90 min. Finally, the black Se was reduced to transparent NaHSe, and white $Na_2B_4O_7$ precipitated.[47,48]

$$4NaBH_4 + 2Se + 7H_2O \leftrightarrow 2NaHSe + Na_2B_4O_7 + 14H_2 \uparrow \quad (1)$$

For the typical synthesis of CMSe-1 QDs with 0.7 : 0.3 molar ratio of Cd : Mo, $Cd(NO_3)_2{\cdot}4H_2O$ (436 mg), $Na_2MoO_4{\cdot}2H_2O$ (147 mg) and TGA (0.5 mL) were dissolved in 200 mL deionized water in a three-neck round bottomed flask with continuous stirring. The pH was adjusted around 11 by 0.1 M NaOH under an N_2 atmosphere to prevent oxidation of the material. The freshly synthesized NaHSe was quickly added into the solution and kept refluxing at 100 °C for 3 h. Furthermore, to synthesize QDs with different molar ratios of Cd : Mo (1 : 0, 0.7 : 0.3, 0.3 : 0.7, and 0 : 1), the compositions of the Cd and Mo precursors were accordingly changed. Scheme 1 depicts the stabilized CMSe alloyed QD in the presence of TGA under reflux conditions.

Photocatalytic H_2O_2 production

The photocatalytic oxygen reduction reactions were performed under 250 W visible light. 20 mg of catalyst was suspended in 20 mL of distilled water containing 5% (v/v) as a sacrificial electron donor. The mixture solution was sonicated for 15 min. Then the suspension was transferred into the reactor and was stirred in the dark with continuous bubbling of O_2 to attain the adsorption–desorption equilibrium. After 30 min, the light was focused on the suspension solutions for 2 h to produce H_2O_2. Then to separate the photocatalyst, the suspension was centrifuged followed by filtration. Further to determine the amount of H_2O_2 produced, the iodometry method was adopted, where 2 mL of 0.1 M KI and 0.05 mL of 0.01 M ammonium molybdate were mixed with 1 mL of filtrate solution. In such a procedure, I^- forms I^{3-} after reacting with H_2O_2 molecules, and the concentration of I^{3-} is measured using a spectrophotometer to determine how much H_2O_2 was produced. Additionally, a blank experiment carried out without the use of a photocatalyst or light and confirming that no H_2O_2 was formed at any concentration confirms the effectiveness of the photocatalyst in the O_2 reduction reaction. UV-vis DRS (λ = 350 nm) was applied to detect the concentration of H_2O_2 produced.

Additionally, the process of decomposing H_2O_2 was conducted in a 30 mL reactor made of quartz, while being exposed to light. In a standard experimental procedure, a reactor was filled with 15 mL of hydrogen peroxide solution (16 mM) and subsequently subjected to cooling through an ice bath. 20 mg of catalyst was introduced into the reactor and subjected to light exposure under continuous agitation. Following the reaction, the solution was centrifuged and subsequent analysis of H_2O_2 was conducted.

Photocatalytic Cr(VI) reduction

CMSe-1 QDs were also used to minimize hazardous Cr(VI) to hypoxic Cr(III) owing to their wide-range light absorption capability and photostability causing serious ecological pollution. From the results of photocatalytic H_2O_2 generation, the highest activity is recorded for CMSe-1 QDs. Therefore, the photocatalytic Cr(VI) reduction was studied using a CMSe-1 catalyst. In the performed experiment, 20 mg of CMSe-1 QDs and 20 mL of 10 ppm Cr(VI) solution were mixed in a beaker. This solution was continuously stirred in the dark for 30 min to attain equilibrium between adsorption and desorption. Subsequently, a 20 W LED was used to illuminate the mixture solution. The photocatalytic reduction of Cr(VI) over CMSe-1 QDs was observed for different times such as 30 min, 60 min,

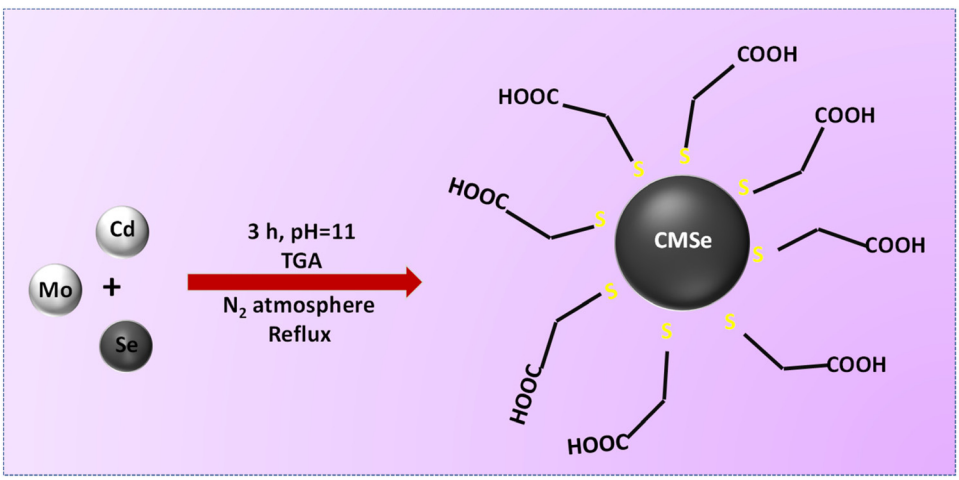

Scheme 1 Schematically illustrating the synthesis procedure of CMSe alloyed QDs.

90 min, and 120 min. The photocatalytic reduction activity of CMSe-1 was also investigated at different pH (3, 6, 9, 12) where the pH was maintained using 1 M HCl and 1 M NaOH. After the reaction, the solution was centrifuged and the supernatant was collected. To prove the photoreduction of Cr(VI) to Cr(III) and quantify the amount of (VI), the colorimetric test was performed, where 2 mL of sulphuric acid (H_2SO_4, 3 M) and 1 mL of freshly prepared 1,5-diphenylcarbonohydrazide (DPC) were added to 2 mL of the supernatant. After allowing it to stand in the dark for 15 min, the absorbance of the solution was measured at 540 nm using a UV-vis spectrophotometer.

Reusability test of CMSe QDs

After photocatalytic reduction, CMSe-1 QDs were recovered by centrifugation and washed several times with ethanol–water solution, and dried under vacuum. Then the QD was directly applied to the next cycles of H_2O_2 generation and Cr(VI) photoreduction.

Results and discussion

Structure and morphology

The powder X-ray diffractometry (XRD) pattern of the synthesized samples (CSe, MSe, CMSe-1, and CMSe-2 QDs with molar ratios 1 : 0, 0 : 1, 0.7 : 0.3, and 0.3 : 0.7 of Cd : Mo[56–58] respectively) is depicted in Fig. 1a. The diffraction peaks obtained from XRD of CMSe-1 and CMSe-2 QDs show peaks of both CdSe and $MoSe_2$ QDs, supporting the formation of an alloyed structure.[49] However, the intensity of the peak depends upon the ratio of Cd : Mo. The peaks of CMSe-1 and CMSe-2 appeared at around 2θ = 25° (111), 42° (220), and 49° (311) with slight shifting (enlarged view depicted in ESI (S1)†) and can be indexed to the characteristic peaks of CdSe with zinc blende structure, which are well matched with previous data (JCPDS Card No. 19-0191). Similarly, the signature peak at 32° corresponds to the characteristic (100) plane of $MoSe_2$ having a rhombohedral structure (JCPDS Card No. 20-0757). It can be seen that evenly dispersed CMSe-1 are tiny dot-like nanoparticles, visualized from TEM images presented in Fig. 1b and c. An average particle size of Σ4 nm was determined from the particle size distribution plot (inset ESI (S2)†). Due to the tendency of QDs to aggregate, the diameter of the CMSe-1 expands. In parallel, Fig. 1d is the high-resolution TEM (HRTEM) image of CMSe-1 that displays a clear crystalline lattice spacing *i.e.*, d = 0.352 nm, which is assigned to the (111) crystal plane and is in good accordance with XRD of CMSe-1. Also, the disordered and unclear areas confined by the yellow circle indicate the presence of defects. Here, in comparison to the lattice fringes of neat CdSe ($d_{spacing}$ = 0.337 nm for the (111) plane), the alloyed CMSe-1 shows a high d spacing value of 0.352 nm for the (111) plane, which indicates lattice expansion and formation of defect or disorder within the system.[50] The polycrystalline structure of CMSe-1 QD can be witnessed from the continuous Deby–Scherrer rings in the selected area electron diffraction (SAED) pattern in Fig. 1e.

Furthermore, XPS analysis was carried out to illustrate the surface chemical state and interfacial electronic states of CMSe-1 QD. Fig. 2a displays Cd 3d spectra, which are deconvoluted into two peaks positioned at binding energies (BEs) of 404.8 and 411.6 eV and are attributed to the Cd $3d_{5/2}$ and Cd $3d_{3/2}$ spin state of Cd(II) respectively.[46,51] The high-resolution deconvoluted Mo 3d spectrum also exhibits two peaks at BEs of 228.6 and 231.6 eV, which are assigned to Mo $3d_{5/2}$ and Mo $3d_{3/2}$ energy levels respectively as shown in Fig. 2b, indicating the +4 oxidation state of Mo.[52] Besides, the peaks at BE of 53.6

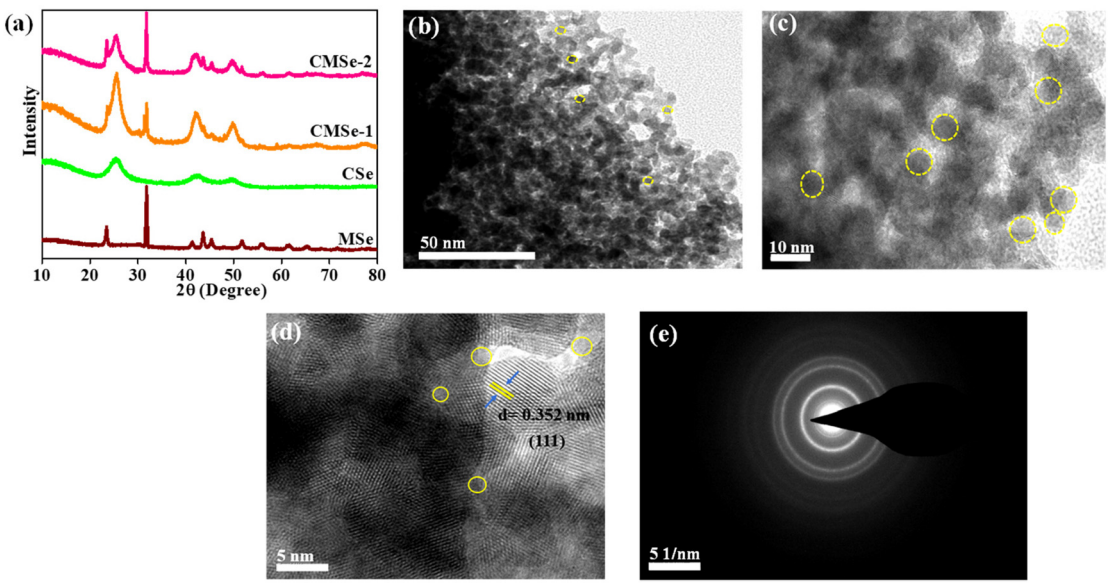

Fig. 1 (a) Powder XRD pattern of CSe, MSe, CMSe-1, and CMSe-2, (b and c) HRTEM images (d) HRTEM fringe pattern (e) SAED pattern of CMSe-1 QD.

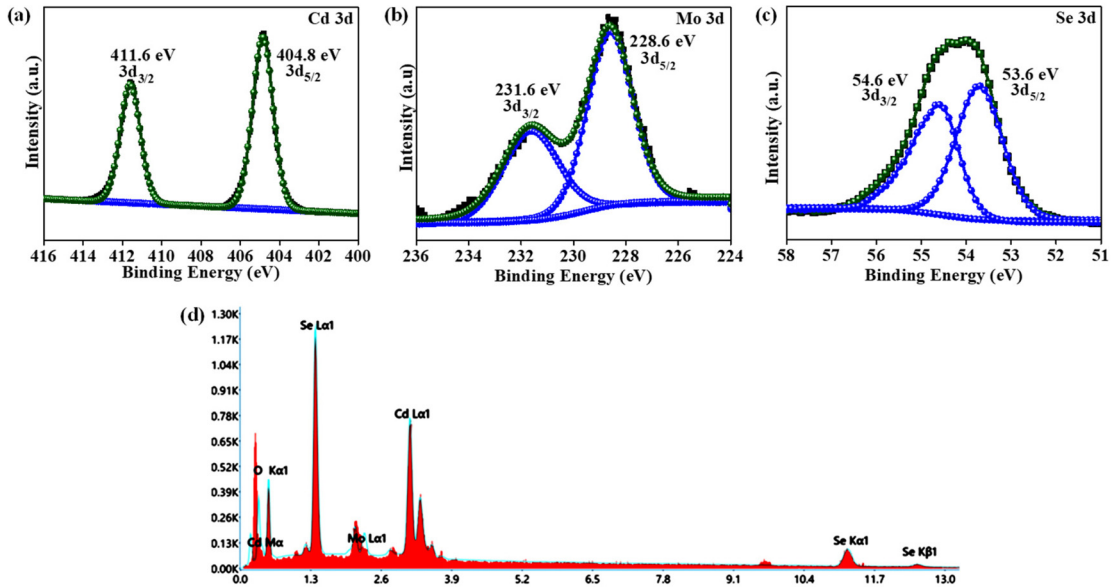

Fig. 2 XPS spectra of (a) Cd, (b) Mo, (c) Se elements, and (d) EDX analysis demonstrating elemental components in CMSe-1.

(Se $3d_{5/2}$) and 54.6 eV (Se $3d_{3/2}$) in Fig. 2c present the (II) oxidation state of Se in the alloyed QD.[53] Moreover, ESI (S3)† presents the survey analysis spectra of CMSe-1 QDs, from which it can be noticed that Cd, Mo, and Se elements are detected, revealing the coexistence of these three elements without any impurity species. In parallel, all the compositional constituents present in CMSe-1 QDs were evaluated from the energy-dispersive X-ray (EDX) (Fig. 2d) study, which is in good accordance with XPS analysis spectra. The color mapping image of CMSe-1 QDs is also included in ESI (S4)† which supports the above observation of elemental content. Additionally, the plotted EPR result in ESI (S5)† shows that the sample CMSe-1 contains a defect with an anisotropic feature brought by super hyperfine splitting.[54] The existence of defects in CMSe-1 systems is also well supported by the HRTEM image (Fig. 1d), crucial for the activation and adsorption of molecular oxygen, which increases the formation of H_2O_2.

Optical and electrochemical properties

The optical absorption properties of CSe, Mse, CMSe-1, and CMSe-2 QDs are also investigated by UV-vis spectroscopy. As depicted in Fig. 3a, the CMSe-1 and CMSe-2 alloyed QDs exhibit good light absorption with their absorption edges in between that of the binary QDs suggesting alloy formation.[55] Moreover, the activity of photocatalysts largely depends on the separation efficiency of electron–hole pairs, which can be estimated by photoluminescence (PL) spectra. Fig. 3b shows the PL spectra of Cse, Mse, CMSe-1, and CMSe-2 QDs photo-excitation at 380 nm, where Mse QDs exhibit the strongest PL intensity due to the highest extent of photogenerated charge carrier recombination. However, the PL intensities of the CMSe-1 and CMSe-2 QDs are notably reduced, indicating that alloying of metals hinders the recombination of charge carriers, and the lowest intensity is seen in CMSe-1 QDs, which is due to the efficient quenching of electron holes. The asymmetric peaks on the PL graph could be caused by band gap transitions and the existence of defects, implying that CMSe-1 QDs like other QDs should have a wide particle size distribution.[36] Additionally, the separation efficiency of electron–hole pairs is also supported by electrochemical impedance spectroscopy (EIS) as illustrated in Fig. 3c. Compared to Cse and Mse QDs, the semi-circular diameter of CMSe-1 and CMSe-2 QDs indicates better charge flow although the smallest arc radius is observed for CMSe-1 QD implying the lowest migration resistance for photo-excited charge carriers. Moreover, Fig. 3d represents the transient photocurrent plot of CSe, MSe, CMSe-1, and CMSe-2 QDs under the light on/off conditions. This implies that the highest transfer efficiency of photogenerated charge carriers is for CMSe-1 QDs, which leads to enhanced photocatalytic activity. Adding more, the small spikes in the photocurrent plot of binary QDs upon interrupted light irradiation indicate the faster recombination of holes and electrons. Additionally, Fig. 3e represents the linear sweep voltammetry (LSV) analysis of the synthesized binary and alloyed QDs with the potential bias range from −0.8 to 0.0 V. All of them exhibit cathodic photocurrent densities and the highest negative photocurrent density (−0.868 mA cm^{-2}) is determined from CMSe-1 QDs, resulting in the most accelerated photogenerated charge carrier separation and hence better activity.

Based on the Bode phase plot of CSe, MSe, CMSe-1, and CMSe-2 QDs, displayed in Fig. 4a, it can be stated that the frequency regions can be used to quickly identify the lifespan of the injected electron. Applying eqn (1), the lifespan of the injected electrons was calculated.

$$\text{The life span of electrons } (\tau) = 1/2\Pi f_{\max} \quad (1)$$

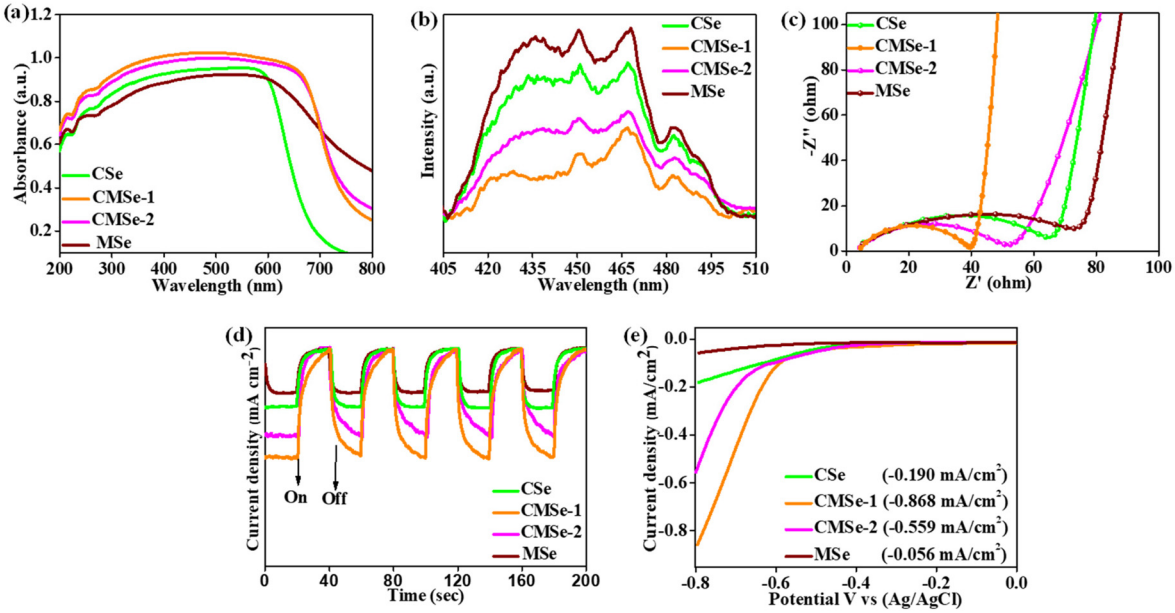

Fig. 3 Analysis of optoelectronic properties of CSe, MSe, CMSe-1, and CMSe-2 by (a) UV-vis DRS absorbance spectra, (b) PL spectra, (c) EIS spectra, (d) transient photocurrent response, (e) linear sweep voltammetry plot.

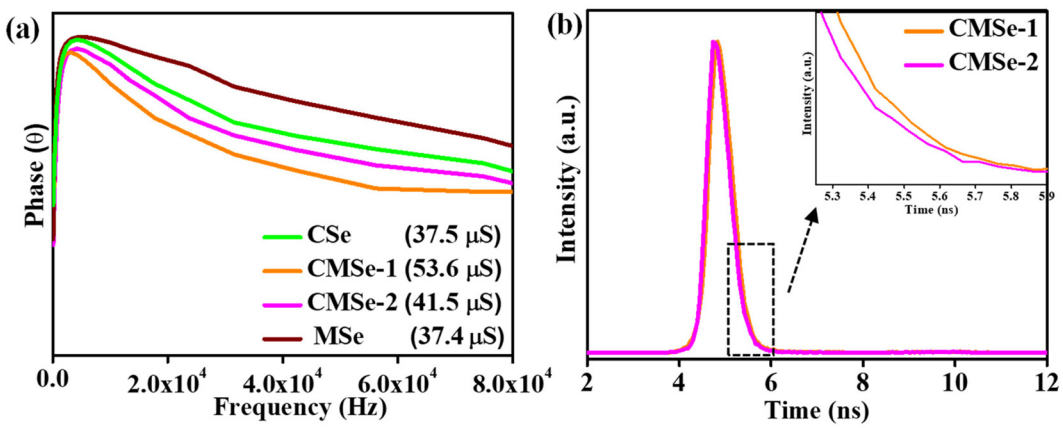

Fig. 4 (a) Bode phase plot of CSe, MSe, CMSe-1, and CMSe-2 (b) TRPL plot of CMSe-1 and CMSe-2.

where τ and f_{max} correspond to the lifetime of photoinjected electrons and the minimum reverse frequency of the photocatalyst. The lifetime of these electrons was somehow correlated with the shift in the peak position along the frequency region *i.e.*, drift to the lower or higher position. In Fig. 4a, CMSe-1 QDs have the lowest frequency value (f_{max}) and longest duration (τ = 53.6 μs) of electron lifespan, resulting in enhanced photocatalytic activity. The photoinjected electron lifespan calculated for CMSe-2, CSe, and MSe are 41.5, 37.5, and 37.4 μs respectively. The substantially longer injected exciton lifespan of CMSe-1 QDs indicates their fast interfacial charge carrier transfer dynamics. Similarly, the time-resolved photoluminescence spectroscopy (TRPL) of the as-prepared CMSe-1 and CMSe-2 QDs was conducted to evaluate the lifespan of photogenerated charge carriers, which is shown in Fig. 4b. A bi-exponential model as specified in eqn (2) was used to fit the acquired decay curves.

$$\text{Fit} = A + \alpha_1 \exp(-t_1/\tau_1) + \alpha_2 \exp(-t_2/\tau_2) \quad (2)$$

where A is a constant and relative contributions are symbolised by α_1 and α_2. The time after a pulsed laser excitation is represented by t. In this context, τ_1 and τ_2 denote the decay lifetimes, respectively, which elucidate the processes of radiative recombination and nonradiative relaxation of photo-excitons.

Using eqn (3) and the parameters listed in Table S1 (ESI†), the average lifetime (τ_{avg}) was calculated.

$$\tau_{avg} = \frac{\alpha_1 {\tau_1}^2 + \alpha_2 {\tau_2}^2}{\alpha_1 \tau_1 + \alpha_2 \tau_2} \quad (3)$$

The CMSe-1 exhibits an average lifetime of 1.53 nanoseconds, surpassing the average lifetime of CMSe-2 (1.51 nanoseconds). This discrepancy suggests that the increased concentration of Cd in CMSe-1 contributes to enhanced exciton dissociation and slow decay of charge carriers on the surface, thereby favourably impacting the photocatalytic activity.

Adding more to the investigation, the Kubelka–Munk function was used to estimate the band gap energy (E_g) of CMSe-1 and CMSe-2 QDs and was found to be 1.76 and 1.70 eV respectively, as illustrated in Fig. 5a. Additionally, the resulting Urbach energies of CMSe-1 and CMSe-2 are determined to be 0.26 eV and 0.19 eV as given in ESI (S6).† Increased disorder or defects in the system are indicated by the high Urbach value of the alloyed CMSe-1 QD. The system becomes more disorderedly, which may be attributed to lattice expansion and, consequently, an increase in Cd concentration may affect the band edge potentials by causing a variation in the band gap energy. Lattice expansion or absence of continuous lattice fringes is related to defect presence. Also, this defect formation is well supported by HRTEM and EPR analysis.[56–58]

Determining the valence band (VB) and conduction band (CB) positions of CMSe-1 and CMSe-2 QDs helps to better explain the mechanism of photocatalytic H_2O_2 production. The flat band potential of CMSe-1 and CMSe-2 QDs were obtained from the Mott–Schottky plots and estimated as −0.60, and −0.53 V (*vs.* Ag/AgCl at pH 7) respectively as shown in Fig. 5b. The positive slopes of the M–S plot evidence CMSe-1 QDs as an n-type semiconductor. The CB minima of CMSe-1 and CMSe-2 are then recalculated by using eqn (4) to be −0.41 and −0.34 eV (*vs.* NHE at pH 7), respectively and their respective VB band positions are 1.35 and 1.37 eV based on eqn (5). Because the CB maximum of CMSe-1 QDs (−0.41 eV, *vs.* NHE) is higher than that of $O_2/{}^{\bullet}O_2^-$(−0.046 V *vs.* NHE), a substantial amount of ${}^{\bullet}O_2^-$ is generated on the CMSe-1 surface which then reacts with H^+ generated by the oxidation process (used sacrificial agent) resulting in more H_2O_2 generation.

$$E_{CB} = E_{Ag/AgCl} - 0.059(7 - \text{pH of the electrolyte}) + E^{\circ}_{Ag/AgCl} \quad (4)$$

$$E_{VB} = E_{CB} + E_g \quad (5)$$

where $E_{Ag/AgCl}$ represents the flat band potential of materials, and the pH of the electrolyte was found to be 6.8, and the reference electrode constant $E^{\circ}_{Ag/AgCl}$ (= 0.198). Likewise, the VB potential of CMSe-1 (1.35 eV) can be evaluated by XPS VB spectroscopy as displayed in Fig. 5c. The primary shoulder pattern of the first peak at the ends with the least binding energy correlates to the VB potential of CMSe-1 in the XPS VB spectra.

Applications

Photocatalytic H_2O_2 generation

The photocatalytic performances of the synthesized QDs were examined towards H_2O_2 generation under visible light irradiation. The concentration of H_2O_2 produced by bare CdSe and $MoSe_2$ QDs are 408.15 μmol g^{-1} h^{-1} and 212.76 μmol g^{-1} h^{-1} respectively. It is notable from Fig. 6a, that CMSe-1 QD reveals the highest H_2O_2 production of 1403.5 μmol g^{-1} h^{-1} which is 3.4 and 6.6 times higher than those of binary CdSe and $MoSe_2$ respectively due to the suppressed exciton recombination rate. CMSe-1 QDs with a Cd/Mo ratio of 0.7/0.3 outperforms CMSe-2 QDs (963 μmol g^{-1} h^{-1}) including binary QD (CdSe and $MoSe_2$). The Cd-rich catalyst (CMSe-1) displays better photocatalytic efficiency than the Mo-rich alloyed QDs (CMSe-2) because the higher proportion of Cd widens the bandgap of CMSe-1 QDs as compared to that of the CMSe-2 QDs. Hence, the electron–hole recombination rate decreases and leads to better activity. Besides, the solar to chemical conversion efficiency (SSC) using CMSe-1 was determined to be 0.27% at $\lambda_{max} \geq 420$ nm using eqn (S1) (detailed formulation in the ESI†). Simultaneously, the decomposition of H_2O_2 becomes a critical issue as it reduces the overall H_2O_2 yield including material loss. Furthermore, from Fig. 6b it can be visualized that by using CMSe-1 as a photocatalyst, the rate of H_2O_2 generation in an O_2-saturated solution is dramatically high, whereas in an N_2 or Ar environment, very negligible H_2O_2 was discovered revealing that O_2 plays a major role in

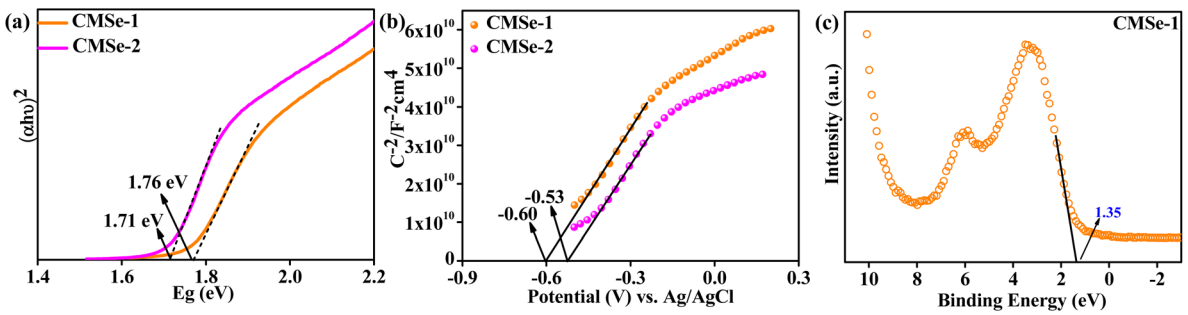

Fig. 5 (a) Tauc plot for the determination of band gap, (b) M–S plot to obtain conduction band potential of CMSe-1 and CMSe-2 QD, (c) XPS VB plot of CMSe-1.

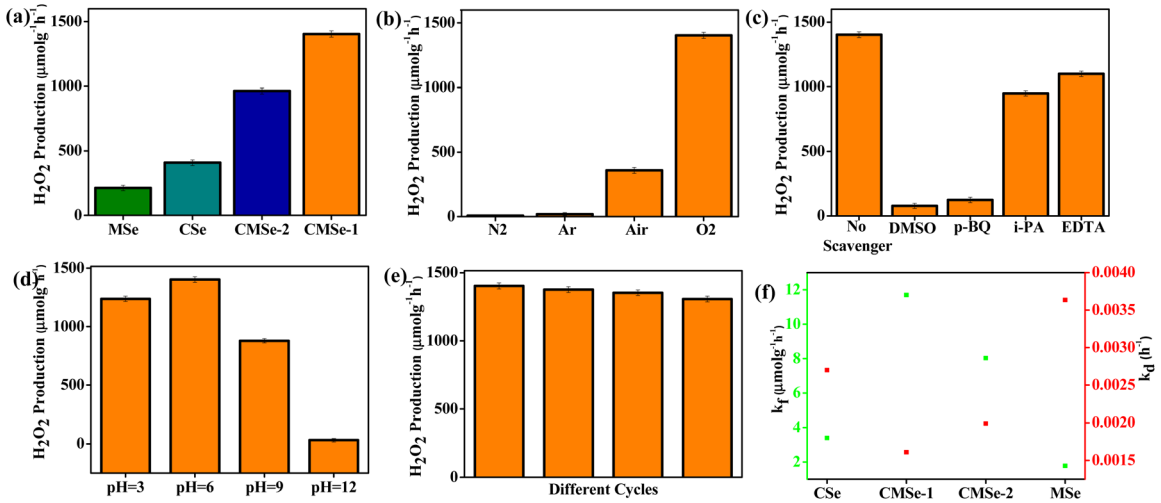

Fig. 6 (a) Yield of photocatalytic H_2O_2 generation using different photocatalysts under 250 W visible light irradiation for 2 h, (b) H_2O_2 production rate under different saturated atmospheres (c) Influence on H_2O_2 generation rate in the presence of different scavengers, (d) The pH effect on the photocatalytic H_2O_2, and (e) reusability plot of CMSe-1, (f) k_f and k_d for H_2O_2 generation rate of photocatalysts (CSe, MSe, CMSe-1, and CMSe-2).

photocatalytic H_2O_2 generation and also confirms the photoreduction of the supplied O_2 to H_2O_2. Additionally, the active species trapping experiments were performed to figure out the reaction pathways of photocatalytic H_2O_2 production using EDTA, dimethyl sulphoxide (DMSO), isopropanol (IPA), and *p*-benzoquinone (BQ) as the scavengers of holes (h^+), electrons (e^-), hydroxyl radical ($OH^\bullet$), and superoxide radical ($^\bullet O_2^-$) respectively. In the absence of a certain sacrificial agent, CMSe-1 demonstrated the best photocatalytic H_2O_2 performance *e.g.*, when EDTA is utilized as the sacrificial agent, the yield of H_2O_2 increases dramatically because it captures holes, allowing more electrons for O_2 reduction. In contrast, employing DMSO, H_2O_2 production reduces significantly, implying the important role of electrons in the O_2 reduction reaction. $^\bullet OH$ and $^\bullet O_2^-$ are trapped by adding IPA and *p*-BQ, respectively. H_2O_2 yield is reduced in the presence of *p*-BQ, but greatly boosted upon the addition of IPA as it is a sacrificial agent. This shows that $^\bullet O_2^-$ rather than $^\bullet OH$ is the active species during H_2O_2 production. Notably, when *p*-BQ or DMSO is added to the solution, there is essentially no H_2O_2 generation indicating that the oxygen reduction reaction is the primary source of H_2O_2 production, which can be confirmed from Fig. 6c. Based on the above observation, it can be projected that O_2 reduction goes predominantly by the superoxide radical mediated single electron two-step route. Further, the superoxide radical generation ability of CMSe-1 QDs is confirmed through the NBT test following our previously reported literature. In this reduction process, alcohol as a sacrificial agent not only oxidizes the holes but also releases H^+ which further interacts with the superoxide intermediate producing H_2O_2. Besides, defect presence in CMSe-1 not only retards the recombination process but encourages O_2 adsorption and activation by lowering the Gibbs free energy of O_2 adsorption (rate-determining stage) promoting hydroperoxy intermediate (*OOH) generation which then transfers to H_2O_2. A similar type of observation was also made by Zou *et al.* and Li *et al.*[59,60] Furthermore, the photoproduction of H_2O_2 under different pH conditions is evaluated and displayed in Fig. 6d. It is observed that at pH 6, the synthesized photocatalyst exhibits the highest catalytic activity. At a lower pH of 3, the catalytic efficiency slightly decreases which might be due to the occurrence of the competitive H_2 evolution reaction. Thereafter, an alkaline medium also hinders the formation of H_2O_2. The reusability of catalyst is an important parameter in deciding its efficacy and practicability. In the present case, four successive cycles of testing were performed on the photocatalytic stability of CMSe-1 QDs. Upon exposure to light for the first three cycles, the ability to generate H_2O_2 is remarkably stable; however, by the fourth cycle, the H_2O_2 concentration had slightly dropped as illustrated in Fig. 6e. The loss of catalyst quantity during recovery and catalyst aggregation due to continued usage is blamed for the reported modest drop in activity during reusability. The remarkable stability is closely related to the supplied XRD of CMSe-1 QD which is nearly identical before and after usage, as shown in ESI (S7).†

Meanwhile, the decomposition of H_2O_2 occurs simultaneously, and this is a competitive reaction involving electrons and holes. The decomposition rate of H_2O_2 with an initial concentration of 1000 μM under light illumination was studied and is shown in ESI (S8).† To analyze the kinetics, the applied eqn (6) and (7) are given below:

$$[H_2O_2] = \left(\frac{k_f}{k_d}\right)(1 - e^{-k_d t}) \quad (6)$$

$$k_d = -dC_t/dt \quad (7)$$

where k_f and k_d represent the formation and decomposition rate constant of H_2O_2, respectively, which combinedly estimate the final H_2O_2 yield. Zeroth and first-order kinetics are applied to determine the value of k_f and k_d respectively. From Fig. 6f, it

is concluded that CMSe-1 having the highest k_f and lowest k_d displays the highest production of H_2O_2 among other samples. The aforementioned observation suggests that enhanced light-harvesting capacity and facilitated charge mobility of CMSe-1 are advantageous for both the photocatalytic formation as well as degradation of H_2O_2. Conversely, the rate of formation of CMSe-1 increases more than the rate of decomposition does, resulting in the overall remarkable rate of H_2O_2 production.

Photocatalytic Cr(VI) reduction

Cr(VI) is grouped under the toxic heavy metal category having carcinogenic effects on bio-diversity; therefore, its elimination or transfer to less toxic Cr(III) form is the most encouraging approach. In this regard, the efficiency of CMSe-1 QDs towards photocatalytic Cr(VI) reduction was carefully examined. However, Cr(VI) does not undergo self-degradation in the presence of light or catalyst only. As depicted in Fig. 7a, 93.6% of Cr(VI) was reduced by CMSe-1 QD within 2 h because of the fastest transfer and separation of charge carriers. Furthermore, a pseudo-first-order kinetic model of CMSe-1 QDs was comprehensively analysed for 2 h showing the rate constant (k) value of 0.0498 for CMSe-1 as shown in Fig. 7b. Moreover, pH is a key factor in Cr(VI) reduction because protons are more readily available at lower pH levels, and the surface of the photocatalyst becomes positively charged and attracts $Cr_2O_7^{2-}$ anions, which speeds up the adsorption process. The redox reaction took place in the solution at higher pH levels, preventing Cr(VI) reduction. In this regard, Fig. 7c illustrates the reduction percentage of Cr(VI) by CMSe-1 at different pH values. The optimum catalytic activity in the photoreduction of Cr(VI) to Cr(III) is observed in acidic pH values (pH = 3) due to the active interaction of Cr anions with cations on the surface of the photocatalysts. Furthermore, the point of zero charges (PZCs) of the CMSe-1 sample was calculated following the drift method as previously reported by our group.[29] The pH_{PZC} value of CMSe-1 QDs is found to be 6.5 from the plot shown in ESI (S9).† Generally, the catalyst surface remains positively charged when the pH of the solution is lower than pH_{PZC}, whereas negatively charged when the pH is higher than pH_{PZC}.[29] Due to acidic pH, Cr anions exist in the $Cr_2O_7^{2-}$ form and as a catalyst with positive charge which favors effective interaction and successful reduction to hypoxic Cr(III). Moreover, a reusability plot of CMSe-1 QDs towards photocatalytic reduction of Cr(VI) is depicted in Fig. 7d which suggests that the catalyst preserved its activity even up to four continuous cycles without any marginal change in performance. Additionally, a comparison table for H_2O_2 production and Cr(VI) reduction of several photocatalysts is presented in Table S2,† which shows the superior activity of CMSe-1 QDs as a single photocatalyst.

Mechanistic approach

The preceding experimental work points to the plausible mechanism depicted in Scheme 2 to have a thorough grasp of

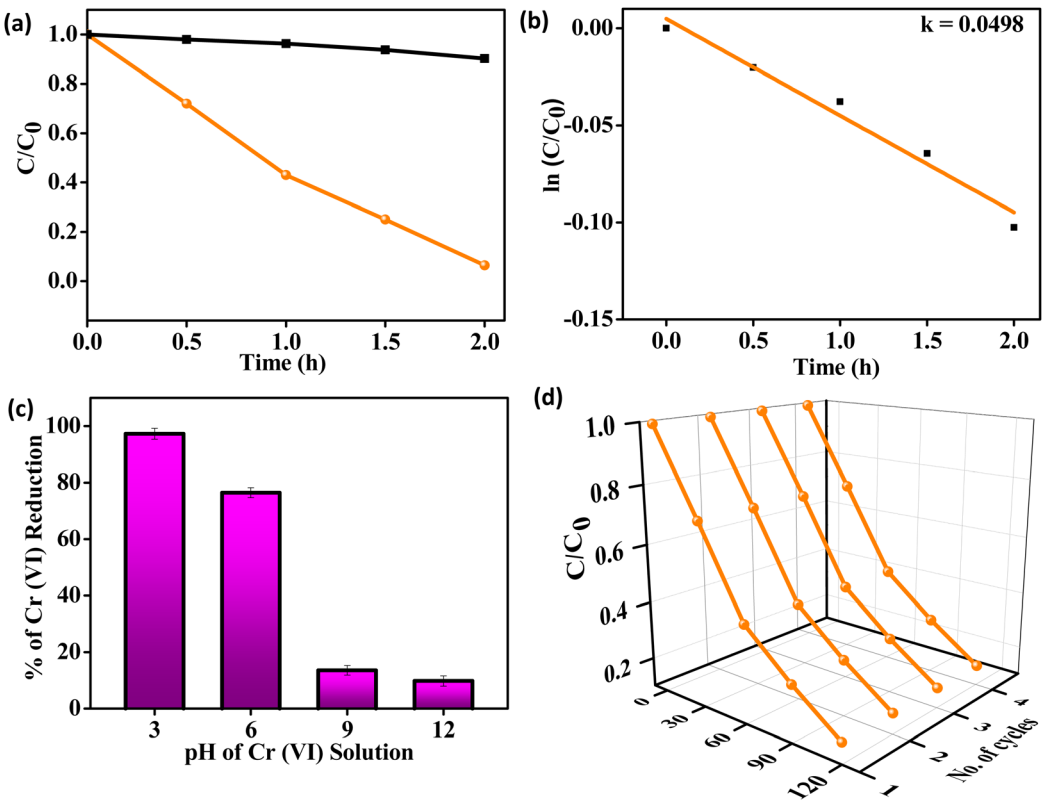

Fig. 7 (a) Photocatalytic Cr(VI) reduction by CMSe-1 under visible light irradiation at various intervals of time, (b) kinetics of first-order mechanism of CMSe-1, (c) comparison of photocatalytic Cr(VI) reduction by CMSe-1 at different pH, (d) reusability test of CMSe-1.

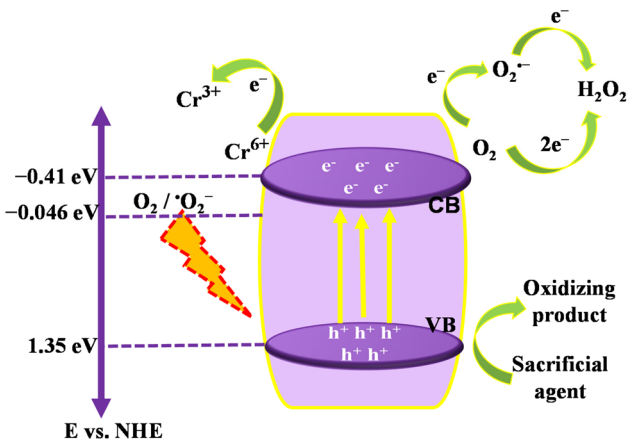

Scheme 2 Plausible mechanism showing separation and migration of photogenerated charge carriers over CMSe-1 QDs for photocatalytic H_2O_2 production and Cr(VI) reduction.

photocatalytic H_2O_2 production and Cr(VI) reduction over the CMSe-1 photocatalyst. In this paper, the band structures of CMSe-1 and CMSe-2 are determined from UV-vis DRS and Mott–Schottky (MS) analysis, and VB-XPS. As the catalyst is exposed to visible light, electrons and holes are produced in the CB and VB respectively. The photogenerated holes in the VB of the CMSe-1 cannot oxidize water because the VB potential of CMSe-1 QD (+1.35 eV) is substantially lower than the necessary potential for water oxidation (2.68 eV).[61] Additionally, H_2O_2 is generated in trials run neither in the dark nor without photocatalysts; hence the O_2 reduction to H_2O_2 by CMSe-1 is likely fuelled by the photocatalytic pathway as represented in the eqn (8)–(12). The dissolved O_2 can be reduced directly by a couple of electrons to generate H_2O_2 (eqn (10)) or by an indirect stepwise route *via* $^{\bullet}O_2^-$ intermediate, which subsequently reacts with protons and electrons to produce H_2O_2 (eqn (11) & (12)). As the necessary condition, the CB of CMSe-1 (−0.41 eV) has enough potential of forming superoxide radicals (−0.046 V *vs.* NHE), further confirmed by NBT analysis (ESI (S10)†). Similarly, the holes in VB of CMSe-1 (+1.35 eV), oxidise the alcohol producing H^+. Previously, from radical scavenger experiments, we confirmed that $^{\bullet}O_2^-$ and e^- play an integral part in the formation of H_2O_2 *via* direct and indirect oxygen reduction channels. Additionally, confirmation regarding the formation of $^{\bullet}O_2^-$ radicals was further obtained by EPR analysis, using 5,5-dimethyl-1-pyrroline *N*-oxide (DMPO) as the spin-trapping reagent. ESI (S11)† shows the peaks of DMPO-$^{\bullet}O_2^-$ under light irradiation. Below mentioned equations reflect the overall steps of H_2O_2 generation.

$$\text{CMSe-1} + h\nu \rightarrow \text{CMSe-1}(e^- + h^+) \quad (8)$$

$$CH_3CH_2OH + 2h^+ \rightarrow CH_3CHO + 2H^+ \quad (9)$$

$$O_2 + 2e^- + 2H^+ \rightarrow H_2O_2 \quad (10)$$

$$O_2 + e^- \rightarrow O_2^{\bullet-} \quad (11)$$

$$O_2^{\bullet-} + e^- + 2H^+ \rightarrow H_2O_2 \quad (12)$$

Additionally, during the photoreduction process of Cr(VI), e^- and h^+ are generated the same way as discussed above. The photogenerated electrons are utilized for the reduction of Cr (VI) and some electrons are engaged in the production of superoxide radicals, which indirectly reduce Cr(VI) to Cr(III).[25] Eqn (13) represents the photoreduction of Cr(VI) to Cr(III):

$$Cr_2O_7^{2-} + 14H^+ + 6e^- \rightarrow 2Cr^{3+} + 7H_2O \quad (13)$$

Conclusion

In summary, it is simple to develop Cd–Mo–Se QDs using the bottom-up reflux approach from their respective precursors at a basic pH under an inert atmosphere with varying Cd and Mo concentrations. TGA is employed as a capping ligand which prevents agglomeration and promotes stabilizing growth. Cd–Mo–Se QDs by significant alloying of Cd and Mo along with defect presence are responsible for this enhancement in their activity. With improved absorption capacity and a lower charge recombination rate, Cd-rich CMSe-1 QDs produce H_2O_2 (1403.5 μmol g^{-1} h^{-1}) at a rate that is significantly higher than that of Mo-rich CMSe-2 QD and binary QDs (CdSe and $MoSe_2$), which is well correlated with optical and electrochemical analysis. The CMSe QDs respond to the production of H_2O_2 in the visible light range where the solar-to-chemical conversion efficiency over CMSe-1 was determined to be 0.27% at $\lambda \geq$ 420 nm. The scavenger test clarifies the superoxide-mediated O_2 reduction route and the efficiency of Cr(VI) reduction over CMSe-1 is reported to be 93.6% in 2 h. Both the reduction of oxygen and the reduction of Cr(VI) follow zero-order kinetics. However, it is discovered that electrons are the primary pertinent active species for H_2O_2 generation and Cr(VI) reduction. CMSe-1 shows noticeable photocatalytic efficiency; however, to further strengthen the performance of the designed material, some modifications can be considered such as cation or anion alloying to prepare quaternary and quinary QDs. Moreover, the recombination rate of excitons can be further lowered by doping and forming heterojunctions of CMSe-1 with other suitable catalysts. These discoveries are crucial for the development of QD photocatalysts in the context of energy conversion and environmental remediation.

Conflicts of interest

The authors declare no competing financial interest.

Acknowledgements

The authors express their profound gratitude toward Siksha 'O' Anusandhan Deemed to be University for giving all the necessary facilities and financial support to carry out this immense research work.

References

1 T. M. Gill, L. Vallez and X. Zheng, The role of bicarbonate-based electrolytes in H_2O_2 production through two-electron water oxidation, *ACS Energy Lett.*, 2021, **6**, 2854–2862.
2 Y. J. Lin, I. Khan, S. Saha, C. C. Wu, S. R. Barman, F. C. Kao and Z. H. Lin, Thermocatalytic hydrogen peroxide generation and environmental disinfection by Bi_2Te_3 nanoplates, *Nat. Commun.*, 2021, **12**, 180.
3 S. A. M. Shaegh, N. T. Nguyen, S. M. M. Ehteshami and S. H. Chan, A membraneless hydrogen peroxide fuel cell using Prussian Blue as cathode material, *Energy Environ. Sci.*, 2012, **5**, 8225–8228.
4 H. Hou, X. Zeng and X. Zhang, Production of hydrogen peroxide by photocatalytic processes, *Angew. Chem., Int. Ed.*, 2020, **59**, 17356–17376.
5 X. Shen, Z. Wang, H. Guo, Z. Lei, Z. Liu and L. Wang, Solvent Engineering of Oxygen–Enriched Carbon Dots for Efficient Electrochemical Hydrogen Peroxide Production, *Small*, 2023, 2303156.
6 J. M. Campos-Martin, G. Blanco-Brieva and J. L. Fierro, Hydrogen peroxide synthesis: an outlook beyond the anthraquinone process, *Angew. Chem., Int. Ed.*, 2006, **45**, 6962–6984.
7 W. Fan, Z. Duan, W. Liu, R. Mehmood, J. Qu, Y. Cao, X. Guo, J. Zhong and F. Zhang, Rational design of heterogenized molecular phthalocyanine hybrid single-atom electrocatalyst towards two-electron oxygen reduction, *Nat. Commun.*, 2023, **14**, 1426.
8 Z. Wang, G. Li, W. Hou, H. Guo, L. Wang and M. Wu, Insights into the Use of Te–O Pairs as Active Centers of Carbon Nanosheets for Efficient Electrochemical Oxygen Reduction, *ACS Nano*, 2023, **17**, 8671–8679.
9 B. He, Z. Wang, P. Xiao, T. Chen, J. Yu and L. Zhang, Cooperative Coupling of H_2O_2 Production and Organic Synthesis over a Floatable Polystyrene–Sphere–Supported TiO_2/Bi_2O_3 S–Scheme Photocatalyst, *Adv. Mater.*, 2022, **34**, 2203225.
10 B. Liu, C. Bie, Y. Zhang, L. Wang, Y. Li and J. Yu, Hierarchically porous ZnO/g-C_3N_4 S-scheme heterojunction photocatalyst for efficient H_2O_2 production, *Langmuir*, 2021, **37**, 14114–14124.
11 Y. Qian, F. Zhang and H. Pang, A Review of MOFs and Their Composites-based Photocatalysts: Synthesis and Applications, *Adv. Funct. Mater.*, 2021, **31**, 2104231.
12 Y. Yang, B. Cheng and J. Yu, TiO_2/In_2S_3 S-scheme photocatalyst with enhanced H_2O_2-production activity, *Nano Res.*, 2023, **16**, 4506–4514.
13 A. Behera, P. Babu and K. Parida, Growth of macroporous TiO_2 on B-doped gC_3N_4 nanosheets: a Z-scheme photocatalyst for H_2O_2 production and phenol oxidation under visible light, *Inorg. Chem. Front.*, 2021, **8**, 1489–1499.
14 B. P. Mishra, L. Biswal, S. Das, L. Acharya and K. Parida, Architecture and Kinetic Studies of Photocatalytic H_2O_2 Generation and H_2 Evolution through Regulation of Spatial Charge Transfer via Z-Scheme Path over a (001) Facet Engineered TiO_2@ MXene/B-g-C_3N_4 Ternary Hybrid, *Langmuir*, 2023, **39**, 957–971.
15 C. Feng, L. Tang, Y. Deng, J. Wang, J. Luo, Y. Liu, X. Ouyang, H. Yang, J. Yuand and J. Wang, Synthesis of leaf–vein–like g–C_3N_4 with tunable band structures and charge transfer properties for selective photocatalytic H_2O_2 evolution, *Adv. Funct. Mater.*, 2020, **30**, 2001922.
16 J. H. Lee, H. Cho, S. O. Park, J. M. Hwang, Y. Hong, P. Sharma, W. C. Jeon, Y. Cho, C. Yang, S. K. Kwak and H. R. Moon, High performance H_2O_2 production achieved by sulfur-doped carbon on CdS photocatalyst via inhibiting reverse H_2O_2 decomposition, *Appl. Catal., B*, 2021, **284**, 119690.
17 W. Ji, Z. Xu, S. Zhang, Y. Li, Z. Bao, Z. Zhao, L. Xie, X. Zhong, Z. Wei and J. Wang, High-efficiency visible-light photocatalytic H_2O_2 production using CdSe-based core/shell quantum dots, *Catal. Sci. Technol.*, 2022, **12**, 2865–2871.
18 D. Prusty, S. Mansingh, N. Priyadarshini and K. M. Parida, Defect Control via Compositional Engineering of Zn-Cu-In-S Alloyed QDs for Photocatalytic H_2O_2 Generation and Micropollutant Degradation: Affecting Parameters, Kinetics, and Insightful Mechanism, *Inorg. Chem.*, 2022, **61**, 18934–18949.
19 K. K. Das, S. Mansingh, R. Mohanty, D. P. Sahoo, N. Priyadarshini and K. Parida, 0D–2D Fe_2O_3/Boron-Doped g-C_3N_4 S-Scheme Exciton Engineering for Photocatalytic H_2O_2 Production and Photo-Fenton Recalcitrant-Pollutant Detoxification: Kinetics, Influencing Factors, and Mechanism, *J. Phys. Chem. C*, 2022, **127**, 22–40.
20 S. Mansingh, D. P. Sahoo, L. Paramanik, M. Sahoo and K. Parida, Robust charge carrier engineering via plasmonic effect and conjugated Π-framework on Au loaded ZnCr-LDH/RGO photocatalyst towards H_2 and H_2O_2 production, *Inorg. Chem. Front.*, 2022, **9**, 559–576.
21 Y. Isaka, Y. Kawase, Y. Kuwahara, K. Mori and H. Yamashita, Two–phase system utilizing hydrophobic metal–organic frameworks (MOFs) for photocatalytic synthesis of hydrogen peroxide, *Angew. Chem.*, 2019, **131**, 5456–5460.
22 S. K. Pradhan, K. Das, R. Bariki, D. Majhi, N. Behera and B. G. Mishra, Facile low temperature reflux synthesis of Bi self-doped Bi_2MoO_6 and construction of $CaFe_2O_4/Bi_2MoO_6$ 0D QD-2D pn heterojunction photocatalyst for efficient bisphenol A degradation and Cr(VI) reduction, *Appl. Surf. Sci.*, 2023, **611**, 155607.
23 A. Dashti, M. Soodi and N. Amani, Cr(VI) induced oxidative stress and toxicity in cultured cerebellar granule neurons at different stages of development and protective effect of R osmarinic acid, *Environ. Toxicol.*, 2016, **31**, 269–277.
24 J. Y. Yue, Y. T. Wang, X. L. Ding, Y. F. Fan, L. P. Song, P. Yang, Y. Ma and B. Tang, Single-atom substitution in donor–acceptor covalent organic frameworks for tunable visible light photocatalytic Cr(VI) reduction, *Mater. Chem. Front.*, 2022, **6**, 3748–3754.

25 S. Mansingh, S. Sultana, R. Acharya, M. K. Ghosh and K. M. Parida, Efficient photon conversion via double charge dynamics CeO_2–$BiFeO_3$ p–n heterojunction photocatalyst promising toward N_2 fixation and phenol–Cr(VI) detoxification, *Inorg. Chem.*, 2020, **59**, 3856–3873.

26 K. K. Das, S. Patnaik, B. Nanda, A. C. Pradhan and K. Parida, $ZnFe_2O_4$–decorated mesoporous Al_2O_3 modified MCM–41: a solar–light–active photocatalyst for the effective removal of phenol and Cr(VI) from water, *ChemistrySelect*, 2019, **4**, 1806–1819.

27 S. Sultana, S. Mansingh and K. M. Parida, Rational design of light induced self healed Fe based oxygen vacancy rich CeO_2 (CeO_2 NS–FeOOH/Fe_2O_3) nanostructure materials for photocatalytic water oxidation and Cr(VI) reduction, *J. Mater. Chem. A*, 2018, **6**, 11377–11389.

28 D. K. Padhi and K. Parida, Facile fabrication of α-FeOOH nanorod/RGO composite: a robust photocatalyst for reduction of Cr(VI) under visible light irradiation, *J. Mater. Chem. A*, 2014, **2**, 10300–10312.

29 D. Kandi, S. Martha, A. Thirumurugan and K. M. Parida, CdS QDs-decorated self-doped γ-Bi2MoO6: a sustainable and versatile photocatalyst toward photoreduction of Cr(VI) and degradation of phenol, *ACS Omega*, 2017, **2**, 9040–9056.

30 J. Yang, Y. Liang, K. Li, G. Yang and S. Yin, One-step low-temperature synthesis of 0D CeO_2 quantum dots/2D BiOX (X = Cl, Br) nanoplates heterojunctions for highly boosting photo-oxidation and reduction ability, *Appl. Catal., B*, 2019, **250**, 17–30.

31 J. Liu, L. Jing, G. Gao, Y. Xu, M. Xie, L. Huang, H. Ji, J. Xie and H. Li, Ag_2S quantum dots in situ coupled to hexagonal SnS_2 with enhanced photocatalytic activity for MO and Cr (VI) removal, *RSC Adv.*, 2017, **7**, 46823–46831.

32 Y. Yu, T. Ma and H. Huang, Semiconducting Quantum Dots for Energy Conversion and Storage, *Adv. Funct. Mater.*, 2023, 2213770.

33 H. Jin, S. Choi, R. Velu, S. Kim and H. J. Lee, Preparation of multilayered CdSe quantum dot sensitizers by electrostatic layer-by-layer assembly and a series of post-treatments toward efficient quantum dot-sensitized mesoporous TiO_2 solar cells, *Langmuir*, 2012, **28**, 5417–5426.

34 H. Yang, Y. Liu, J. Hao, H. Tang, S. Ding, Z. Wang, F. Fang, D. Wu, W. Zhang, H. Liu and B. Xu, Alloyed green-emitting CdZnSeS/ZnS quantum dots with dense protective layers for stable lighting and display applications, *ACS Appl. Mater. Interfaces*, 2021, **13**, 32217–32225.

35 J. Sahu, D. Prusty, S. Mansingh and K. Parida, A review on alloyed quantum dots and their applications as photocatalysts, *Int. J. Hydrogen Energy*, 2023, **48**, 29097–29118.

36 D. Kandi, S. Martha, A. Thirumurugan and K. M. Parida, Modification of BiOI microplates with CdS QDs for enhancing stability, optical property, electronic behavior toward rhodamine B decolorization, and photocatalytic hydrogen evolution, *J. Phys. Chem. C*, 2017, **121**, 4834–4849.

37 D. Kandi, D. P. Sahoo, S. Martha and K. Parida, Rational Design of a Coupled Confronting Z–Scheme System Toward Photocatalytic Refractory Pollutant Degradation and Water Splitting Reaction, *Adv. Mater. Interfaces*, 2019, **6**, 1900370.

38 D. Prusty, S. Mansingh and K. M. Parida, Synthesis of Z-schemes 0D–3D heterojunction bi-functional photocatalyst with ZnInCuS alloyed QDs supported BiOI MF for H_2O_2 production and N_2 fixation, *Catal. Sci. Technol.*, 2023, **13**, 1311–1324.

39 D. Prusty, S. Mansingh, K. K. Das, J. Sahu and K. M. Parida, Non-stoichiometric $Cu_xIn_{1-x}S$ quantum dots for robust photodegradation of gemifloxacin: influencing parameters, intermediates, and insights into the mechanism, *Adv. Environ. Sci.*, 2022, **1**, 769–780.

40 Y. Nosaka and A. Y. Nosaka, Generation and detection of reactive oxygen species in photocatalysis, *Chem. Rev.*, 2017, **117**, 11302–11336.

41 S. Lin, N. Zhang, F. Wang, J. Lei, L. Zhou, Y. Liu and J. Zhang, Carbon vacancy mediated incorporation of Ti_3C_2 quantum dots in a 3D inverse opal g-C_3N_4 schottky junction catalyst for photocatalytic H_2O_2 production, *ACS Sustainable Chem. Eng.*, 2020, **9**, 481–488.

42 P. Ma, X. Zhang, C. Wang, Z. Wang, K. Wang, Y. Feng, J. Wang, Y. Zhai, J. Deng, L. Wang and K. Zheng, Band alignment of homojunction by anchoring CN quantum dots on g-C_3N_4 (0D/2D) enhance photocatalytic hydrogen peroxide evolution, *Appl. Catal., B*, 2022, **300**, 120736.

43 J. Xiong, X. Li, J. Huang, X. Gao, Z. Chen, J. Liu, H. Li, B. Kang, W. Yao and Y. Zhu, CN/rGO@ BPQDs high-low junctions with stretching spatial charge separation ability for photocatalytic degradation and H_2O_2 production, *Appl. Catal., B*, 2020, **266**, 118602.

44 J. Xu, Q. Ji, Y. Wang, C. Wang and L. Wang, Enhanced photocatalytic H_2/H_2O_2 production and tetracycline degradation performance of CdSe quantum dots supported on K, P, N-co-doped hollow carbon polyhedrons, *Chem. Eng. J.*, 2021, **426**, 130808.

45 D. Prusty, L. Paramanik and K. Parida, Recent advances on alloyed quantum dots for photocatalytic hydrogen evolution: a mini-review, *Energy Fuels*, 2021, **35**, 4670–4686.

46 J. Han, Y. Liu, F. Dai, R. Zhao and L. Wang, Fabrication of CdSe/$CaTiO_3$ nanocomposties in aqueous solution for improved photocatalytic hydrogen production, *Appl. Surf. Sci.*, 2018, **459**, 520–526.

47 D. L. Klayman and T. S. Griffin, Reaction of selenium with sodium borohydride in protic solvents. A facile method for the introduction of selenium into organic molecules, *J. Am. Chem. Soc.*, 1973, **95**, 197–199.

48 W. Schumacher, A. Nagy, W. J. Waldman and P. K. Dutta, Direct synthesis of aqueous CdSe/ZnS-based quantum dots using microwave irradiation, *J. Phys. Chem. C*, 2009, **113**, 12132–12139.

49 E. Aslan, O. Birinci, A. Aljabour, F. Özel, I. Akın, I. Hatay Patir, M. Kus and M. Ersoz, Photocatalytic Hydrogen Evolution by Oleic Acid–Capped CdS, CdSe, and $CdS_{0.75}Se_{0.25}$ Alloy Nanocrystals, *ChemPhysChem*, 2014, **15**, 2668–2671.

50 X. Liu, C. Ma, Y. Yan, G. Yao, Y. Tang, P. Huo, W. Shi and Y. Yan, Hydrothermal synthesis of CdSe quantum dots and their photocatalytic activity on degradation of cefalexin, *Ind. Eng. Chem. Res.*, 2013, **52**, 15015–15023.

51 Y. Wang, J. Peng, Y. Xu, H. Bai, R. Zhao, J. Han and L. Wang, Hollow In_2O_3 nanotubes decorated with $Cd_{0.67}Mo_{0.33}Se$ QDs for enhanced photocatalytic hydrogen production performance, *Int. J. Hydrogen Energy*, 2021, **46**, 30393–30401.

52 T. Zhao, Z. Xing, Z. Xiu, Z. Li, S. Yang and W. Zhou, Oxygen-doped MoS_2 nanospheres/CdS quantum dots/g-C_3N_4 nanosheets super-architectures for prolonged charge lifetime and enhanced visible-light-driven photocatalytic performance, *ACS Appl. Mater. Interfaces*, 2019, **11**, 7104–7111.

53 L. K. Putri, B. J. Ng, W. J. Ong, H. W. Lee, W. S. Chang, A. R. Mohamed and S. P. Chai, Energy level tuning of CdSe colloidal quantum dots in ternary 0D-2D-2D CdSe QD/B-rGO/O-gC_3N_4 as photocatalysts for enhanced hydrogen generation, *Appl. Catal., B*, 2020, **265**, 118592.

54 Q. Chen, H. Zhang, Y. Feng and B. Miao, High polarizability enhanced EPR, optical linear & nonlinear and electric conductivity: Role of NiFe2O4 nanocrystals in transparent tellurite glass-ceramics, *J. Alloys Compd.*, 2023, **930**, 167394.

55 X. B. Fan, S. Yu, F. Zhan, Z. J. Li, Y. J. Gao, X. B. Li, L. P. Zhang, Y. Tao, C. H. Tung and L. Z. Wu, Nonstoichiometric Cu_xIn_yS quantum dots for efficient photocatalytic hydrogen evolution, *ChemSusChem*, 2017, **10**, 4833–4838.

56 Y. Bai, H. Zhang, B. Xiang, X. Liang, J. Hao, C. Zhu and L. Yan, Selenium defect boosted electrochemical performance of binder-free VSe_2 nanosheets for aqueous zinc-ion batteries, *ACS Appl. Mater. Interfaces*, 2021, **13**, 23230–23238.

57 S. Mansingh, S. Subudhi, S. Sultana, G. Swain and K. Parida, Cerium-based metal–organic framework nanorods nucleated on CeO_2 nanosheets for photocatalytic N_2 fixation and water oxidation, *ACS Appl. Nano Mater.*, 2021, **4**, 9635–9652.

58 C. Zhang, Y. Xu, C. Lv, L. Bai, J. Liao, Y. Zhai, H. Zhang and G. Chen, Amorphous engineered cerium oxides photocatalyst for efficient nitrogen fixation, *Appl. Catal., B*, 2020, **264**, 118416.

59 B. Liu, J. Du, G. Ke, B. Jia, Y. Huang, H. He, Y. Zhou and Z. Zou, Boosting O_2 reduction and H_2O dehydrogenation kinetics: surface N–hydroxymethylation of g–C_3N_4 photocatalysts for the efficient production of H_2O_2, *Adv. Funct. Mater.*, 2022, **32**, 2111125.

60 R. An, Y. Zhao, H. Bai, L. Wang and C. Li, Decoration of Au NPs on hollow structured BiOBr with surface oxygen vacancies for enhanced visible light photocatalytic H_2O_2 evolution, *J. Solid State Chem.*, 2022, **306**, 122722.

61 H. Fattahimoghaddam, T. Mahvelati-Shamsabadi and B. K. Lee, Enhancement in photocatalytic H_2O_2 production over g-C_3N_4 nanostructures: a collaborative approach of nitrogen deficiency and supramolecular precursors, *ACS Sustainable Chem. Eng.*, 2021, **9**, 4520–4530.